Nanoscale Advances

PAPER

View Article Online
View Journal | View Issue

Check for updates

Cite this: *Nanoscale Adv.*, 2020, **2**, 4822

Received 8th June 2020
Accepted 21st August 2020

DOI: 10.1039/d0na00462f

rsc.li/nanoscale-advances

5-Ammoniumvaleric acid stabilized mixed-dimensional perovskite submicron platelets with white light emission†

Yamin Shi,‡ Jiarui Hu,‡ Jian Chen, Yaxin Xu, Wantian Yang, Junnian Chen* and Yunbin He *

Low-dimensional Pb–Br and Pb–Cl perovskite single crystals have aroused considerable attention due to their broadband white-light emission. But their synthesis involving halogenation of organic amines, dissolution of lead oxide and a slow cooling process is quite complicated. Herein, we report white light emission from mixed-dimensional AVA$_x$(MAPbCl$_3$) perovskite submicron platelets formed by one-step solution processing. It is found that the presence of 5-ammoniumvaleric acid (5-AVA) with a zwitterionic functional group is crucial for modulating the morphology and structural dimensionality of perovskites. Importantly, AVA$_x$(MAPbCl$_3$) perovskites exhibit distinctive structural dimensionality dependent broadband emission, indicating the formation of self-trapped excited states. The AVA$_2$(MAPbCl$_3$) perovskite exhibits white-light emission with a color rendering index (CRI) of 85 and a correlated color temperature (CCT) of 8624 K, yielding "cold" white light. Moreover, the mixed-dimensional perovskite exhibits good stability for more than 30 days. With this report, we aim to provide a facile approach for synthesizing stable low-dimensional perovskite nanostructures for making advanced optoelectronic devices.

1. Introduction

Organic–inorganic hybrid perovskites hold promise as a new generation of semiconductors that combine the advantages of high mobility of an inorganic semiconductor with facile processing of an organic molecule. These perovskites have attracted considerable interest in solar cell and light-emitting fields on account of high solar cell efficiency[1–4] and external quantum efficiency.[5,6] Nevertheless, the further advancement of the leading three dimensional (3D) perovskites is hindered by their intrinsic instability. Accordingly, molecule engineering is carried out to explore stable perovskites. Among the alternative materials, two-dimensional (2D) $(C_nH_{2n+1}NH_3)_2PbX_4$ perovskites with hydrophobic large cations occupying A-sites turn out to be the most favorite type.[7–9] Typically, 2D perovskites are more versatile than 3D perovskites due to the higher structure tolerance and tunable quantum well layers. The highly tunable structure components endow them with versatile optical and electrical properties to design materials for specific applications.

Recently, two-dimensional Pb–Br and Pb–Cl white-light emitters have gained great attention in the solid-state lighting field.[10–13] These newly emerged single-phase 2D perovskites are promising candidates for current commercial multi-source white-light emitters as a result of the high color stability and facile processing. Additionally, the white-light emission could be tuned over a wide range from cold white to warm white by manipulation of the functional organic cations, halide anions and the number of inorganic semiconductor quantum well layers. Karunadasa *et al.* have carried out pioneering work on developing 2D perovskite white-light emitters in 2014.[10] They reported (110) orientated white-light emitting perovskites featuring a corrugated perovskite layer, including (EDBE)PbX$_4$ (X = Cl, Br) and (*N*-MEDA)PbBr$_4$. Mechanistic investigations have revealed that the white-light emission originates from transient self-trapped excitons (STEs) formed by large lattice deformations associated with strong electron–phonon coupling. Later, white-light emission has also been observed in 2D (001)-oriented perovskites such as (4amp)PbBr$_4$,[12] $(C_6H_{11}NH_3)_2PbBr_4$ (ref. 14) and $(C_6H_5C_2H_4NH_3)_2PbCl_4$.[15] The broadband emission resulted from the STEs generated in highly distorted local Pb–X octahedra as well. Besides these diammonium and cyclic ammonium based perovskites, simple alkyl ammonium based perovskites such as $EA_4Pb_3Br_{10-x}Cl_x$

Ministry-of-Education Key Laboratory for the Green Preparation and Application of Functional Materials, Hubei Key Laboratory of Polymer Materials, School of Materials Science & Engineering, Hubei University, Wuhan 430062, P. R. China. E-mail: chenjunnian910@hubu.edu.cn; ybhe@hubu.edu.cn

† Electronic supplementary information (ESI) available: Optical microscopy images of AVA$_x$(MAPbCl$_3$) perovskites. XRD, SEM and AFM characterization of the microstructure and morphology of 2D (AVA)$_2$PbCl$_4$ perovskites. Time-dependent PL and XRD analyses of the stability of AVA$_x$(MAPbCl$_3$) perovskites. See DOI: 10.1039/d0na00462f

‡ Yamin Shi and Jiarui Hu contributed equally to this work.

and $(C_4H_9NH_3)_2PbCl_4$ also exhibited intrinsic white-light emission.[16,17] Despite the robust progress in exploring 2D perovskite white-light emitters, developing facile methods for the synthesis is still a challenge. Moreover, the search for novel perovskites with high stability for white-light emission is underway.

Herein, we report a one-step solution process for the facile preparation of low-dimensional perovskites by employing zwitterionic 5-ammoniumvaleric acid (5-AVA) as a structure-directing agent to *in situ* tailor a 3D $MAPbCl_3$ perovskite into a mixed-dimensional $AVA_x(MAPbCl_3)$ perovskite. The introduction of 5-AVA into the perovskite precursor produces mixed-dimensional perovskites featuring a submicron-scale structure. It turns out that the employment of zwitterionic 5-AVA molecules without halogenation greatly simplified the synthesis and retained the tailoring function of the halogenated 5-AVA cations.[18] As the structural dimensionality of the perovskite decreases from 3D to mixed-dimensional, *i.e.*, a predominant 2D phase mixed with a 3D phase, the photoluminescence (PL) of the $AVA_x(MAPbCl_3)$ perovskite evolves from narrow band-edge emission along with multiple defect-state emission to broadband white emission, indicating structure-dimensionality dependent broadband emission. Besides, the $AVA_2(MAPbCl_3)$ perovskite exhibits white-light emission with a color rendering index (CRI) of 85 and a correlated color temperature (CCT) of 8624 K. Moreover, it is proposed that 5-AVA bonded to Pb^{2+} ions slows down the vertical growth rate and yields perovskites with a submicron in-plane size. And an exchange–exfoliation mechanism is proposed for understanding the formation of mixed-dimensional perovskites. Furthermore, the long-term stability of the $AVA_2(MAPbCl_3)$ perovskite is investigated by conducting time-dependent structure and photoluminescence measurements.

2. Experimental

Materials

5-Aminovaleric acid, 4-amino-1-butanol, glutaric acid and dimethyl sulfoxide (DMSO) were purchased from Aladdin Industrial Inc. $PbCl_2$ was purchased from Wuhan Jingge Co., Ltd. Citric acid was bought from Sinopharm Chemical Reagent Co., Ltd. Methylamine (MA) and HCl were purchased from Sigma-Aldrich Co. LLC. The methylamine salt (MACl) was synthesized by reacting methylamine (MA) with HCl, followed by purification and recrystallization with ether and ethanol.

Synthesis of 5-ammoniumvaleric acid stabilized methylammonium lead chloride ($AVA_x(MAPbCl_3)$)

A $MAPbCl_3$ perovskite precursor solution was prepared by dissolving $PbCl_2$ and MACl with a molar ratio of 2 : 3 in 1 mL of dimethyl sulfoxide (DMSO), and stirring at 80 °C for 2 h under ambient conditions. Then, we added 5-ammoniumvaleric acid (AVA) into the $MAPbCl_3$ precursor solution at different molar ratios, resulting in several $AVA_x(MAPbCl_3)$ compositions (x = 0.125, 0.25, 1, and 2). Next, the perovskite films were prepared by blade-coating 50 μL of the precursor solution onto glass slides and annealing at 100 °C.

Synthesis of 5-ammoniumvaleric acid lead chloride (AVA_2PbCl_4)

Besides, an AVA_2PbCl_4 perovskite thin film was prepared for reference. Briefly, white AVACl crystals were synthesized from the reaction of 5 mL of 5-aminovaleric acid (97%) and 5 mL of HCl (37 wt% in water) in 12.5 mL of methanol (AR) at 0 °C. An AVA_2PbCl_4 perovskite precursor was prepared by dissolving AVACl and $PbCl_2$ with a molar ratio of 2 : 1 in DMSO. Next, the perovskite films were prepared by blade-coating the AVA_2PbCl_4 perovskite precursor solution onto glass slides and annealing at 100 °C.

Characterization

The morphologies of the perovskites were characterized using an optical microscope (BX51, OLYMPUS), scanning electron microscope (JSM6510LV, Japan) and atomic force microscope (Multimode 8, Burke). X-ray diffraction (XRD) patterns of the samples were obtained using an XRD diffractometer (BRUKER D8 ADVANCE). The optical absorption spectra were measured on a UV-Vis-NIR spectrophotometer (UV-3600 Plus, Shimadzu) by using a deuterium lamp and a bromide–tungsten lamp as the light source. The Raman and PL spectra of the perovskites were measured using a confocal Raman/PL system (HR-800, HORIBA Jobin Yvon) at an excitation wavelength of 325 nm with a light intensity of 500 μW cm^{-2}. The PL lifetimes of $(AVA)_2PbCl_4$ and $AVA_2(MAPbCl_3)$ perovskites were obtained using a Raman microscope (WITec-alpha 300) at room temperature.

3. Results and discussion

Chloride is widely employed as a dopant in $MAPbI_3$ and $MAPbBr_3$ perovskites for obtaining high photovoltaic[19–21] and light-emission performance.[22,23] However, the synthesis requiring halogenation of organic amines, dissolution of lead oxide and a slow cooling process remains challenging. Herein, we develop a facile approach for synthesizing mixed-dimensional lead chloride perovskites (Fig. 1a). In the novel configuration, bilayers of zwitterionic $^+NH_3C_4H_9COO^-$ molecules separate the 3D $MAPbCl_3$ network by forming coordination interactions between deprotonated COO^- and Pb atoms.[24] This configuration is referred to as the $AVA_x(MAPbCl_3)$ perovskite (x = 0.125, 0.25, 1, and 2), where x represents the molar ratio of 5-AVA to $MAPbCl_3$. Notably, with increasing x value, a higher fraction of the mono-layered 2D perovskite phase is expected to be achieved in the mixed-dimensional perovskites. As illustrated in Fig. 1b, the mixed-dimensional perovskite naturally forms an alternating stacked quantum well structure, where an inorganic semiconductor layer and an organic cation layer act as a quantum well layer and a barrier layer, respectively. It should be noted that the mixed-dimensional perovskites described here consist of 2D mono-layered and 3D perovskites. Due to the mismatch of the band gap and the dielectric constant in the inorganic and organic components, the 2D perovskite exhibits strong quantum confinement and dielectric confinement effects. We then carried out XRD and Raman measurements to determine the actual structure of our

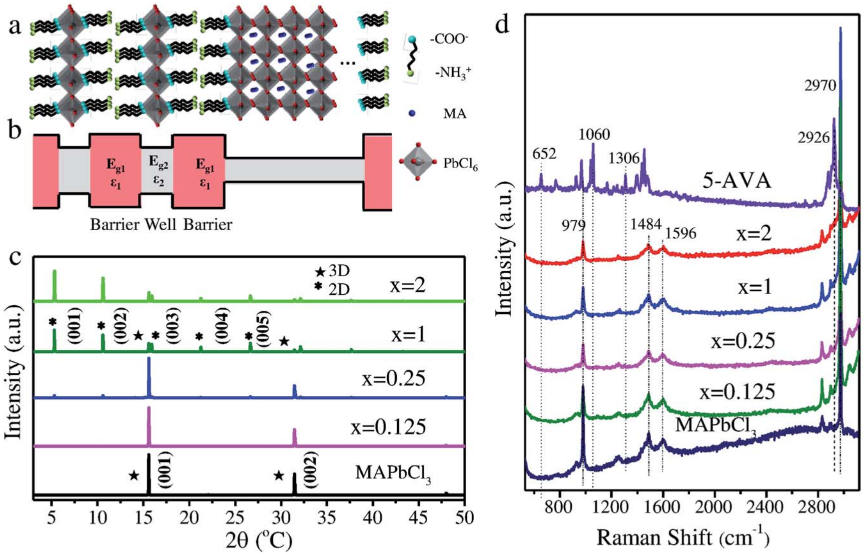

Fig. 1 (a) Schematic crystal structure of the mixed-dimensional $AVA_x(MAPbCl_3)$ perovskite, which is a mixed 2D/3D perovskite. (b) Schematic energy diagram showing multiple quantum wells in the $AVA_x(MAPbCl_3)$ perovskite. (c) XRD patterns of $MAPbCl_3$ and $AVA_x(MAPbCl_3)$ perovskites. (d) Raman spectra of 5AVA, $MAPbCl_3$ and $AVA_x(MAPbCl_3)$ perovskites.

synthesized samples. The XRD patterns of $MAPbCl_3$ and $AVA_x(MAPbCl_3)$ perovskites are presented in Fig. 1c. For clarity, we distinguished the diffraction peaks of the 2D and 3D phases with different symbols. Typically, the $MAPbCl_3$ perovskite adopts the cubic phase, as confirmed by the XRD measurement, with two main diffraction peaks located at 15.6° and 31.4° corresponding to the (001) and (002) lattice planes of the 3D phase,[25] respectively. The $AVA_{0.125}(MAPbCl_3)$ perovskite still exhibits the characteristic diffraction pattern of the 3D phase, indicating nonoccurrence of structural transformation upon incorporation of a small amount of 5-AVA. As x increases to 0.25, the $AVA_{0.25}(MAPbCl_3)$ perovskite shows typical 3D diffraction peaks accompanied by a set of nearly equally spaced weak diffraction peaks. This set of diffraction peaks can be indexed as (00*l*) crystal planes of a layered 2D structure stacked parallel to the substrate, indicating that the 3D perovskites were partly transformed into 2D perovskites.[26] Further increase of x to 1 and 2 leads to a significant decrease in the 3D characteristic diffraction peaks and a dramatic rise in 2D diffraction peaks, suggesting that the dimensionality transformation is much enhanced at higher 5-AVA contents. These observations reveal that the $AVA_x(MAPbCl_3)$ ($x = 0.25$, 1, and 2) perovskites formed in this work are always a mixture of a 2D mono-layered phase and a 3D phase with varying volume ratio depending on the 5-AVA content of x. While the 3D perovskite phase remains predominant in $AVA_{0.25}(MAPbCl_3)$, the 2D phase overwhelms in $AVA_x(MAPbCl_3)$ with higher 5-AVA contents ($x = 1$ and 2). From the 3D phase to the 2D phase, the (001) peak position shifts from 15.6° to 5.3°, indicating a huge expansion of the interlayer spacing as a result of 5-AVA molecular layer intercalation. However, due to the persistent presence of the 2D mono-layered phase in $AVA_x(MAPbCl_3)$ ($x = 0.25$, 1, and 2), the characteristic low-angle diffraction peak of (001) appears at a fixed 2θ angle of 5.3° independent of x; this differs evidently from the previously reported 2D/3D $AVA(MAPbBr_3)_n$ perovskites, in which quasi-2D phases containing different numbers of Pb–Br octahedral layers give rise to (001) diffraction peaks at varying low angles.[24] The Raman spectra of 5-AVA powder, $MAPbCl_3$ and $AVA_x(MAPbCl_3)$ perovskites are shown in Fig. 1d. For the $AVA_x(MAPbCl_3)$ perovskites, the characteristic peaks of 5-AVA at 652, 1060 and 1306 cm^{-1} were too weak to be detected. Obviously, the strong Raman peak at 2926 cm^{-1} can be assigned as the characteristic peak for 5-AVA, since it is not observed in the 3D $MAPbCl_3$ perovskite. As the content of 5-AVA increases, $AVA_x(MAPbCl_3)$ perovskites show a remarkable shoulder peak around 2926 cm^{-1}, indicating that 5-AVA has been incorporated into the 3D $MAPbCl_3$ perovskite. The incorporation of 5-AVA further drives the transformation of the 3D $MAPbCl_3$ perovskite into 2D mono-layered perovskites. Conversely, the Raman peaks at 979, 1484, 1596 and 2970 cm^{-1}, which are related to the rotation and vibration of MA^+, are retained in the $AVA_x(MAPbCl_3)$ perovskites. Besides, the relative Raman peak intensities of MA^+ are highly dependent on the x values. With the increase of x, the intensity of the MA-related Raman peak located at 979 cm^{-1} decreases continually, indicating that more MA species are released from 3D $MAPbCl_3$ perovskites during the 3D to 2D structural transformation. This phenomenon further indicates that more 3D perovskites have been transformed into 2D perovskites. Moreover, the MA-related Raman peak at 979 cm^{-1} is also observed in the $AVA_2(MAPbCl_3)$ perovskite, suggesting that the 3D phase is somewhat retained, which is consistent with above XRD results.

Morphology measurements of $AVA_x(MAPbCl_3)$ perovskites were further conducted to understand the 5-AVA directed morphology evolution. The 3D $MAPbCl_3$ perovskite, identified from optical microscopy images (Fig. S1†), exhibits a cubic morphology with a pyramidal structure in the center. AVA_x(-$MAPbCl_3$) perovskites display a morphology of discrete submicron platelets. Fig. 2 presents the scanning electron microscopy (SEM) images of the 3D $MAPbCl_3$ perovskites and the $AVA_x(MAPbCl_3)$ perovskites. Obviously, the 3D $MAPbCl_3$ perovskites display a bulk cubic structure with lateral dimensions up to ∼100 μm (Fig. 2a), while the $AVA_x(MAPbCl_3)$ perovskites show a submicron platelet structure. As x increases from 0.125 to 1, the crystal size of perovskites decreases from ∼20 to 1 μm (Fig. 2b–d). As x further increases up to 2, the lateral size of perovskites further decreases down to hundreds of nanometers (Fig. 2e). The thickness of an $AVA_2(MAPbCl_3)$ perovskite submicron platelet is determined to be ∼100 nm by atomic force microscopy (AFM) measurement (Fig. 2f). The observation of x-dependent lateral size and thickness of $AVA_x(MAPbCl_3)$ perovskites strongly indicates a 5-AVA directed growth mode, which will be discussed later.

We then performed absorption and PL measurements to gain a deep understanding of the structural dimensionality dependent optical properties of the $AVA_x(MAPbCl_3)$ perovskites. The absorption spectra of $MAPbCl_3$ and $AVA_x(MAPbCl_3)$ perovskites are presented in Fig. 3a. Typically, the $MAPbCl_3$ perovskite displays an intrinsic absorption onset at ∼420 nm (2.95 eV). $AVA_x(MAPbCl_3)$ perovskites with $x = 0.125$ and 0.25 retain the band-edge absorption feature of 3D $MAPbCl_3$ perovskites. As x increases to 1 and 2, the $AVA_x(MAPbCl_3)$ perovskites display typical 3D band-edge absorption and 2D exciton absorption features, confirming the formation of mixed-dimensional perovskites. Both $AVA(MAPbCl_3)$ and $AVA_2(MAPbCl_3)$ perovskites show a feature exciton absorption peak at around 329 nm (3.77 eV), which is attributable to the 2D perovskite phase. As discussed above, the mixed-dimensional $AVA_x(MAPbCl_3)$ perovskites are all composed of 2D and 3D perovskites with the 2D mono-layered phase predominating at high 5-AVA contents of $x = 1$ and 2. Therefore, all the $AVA_x(MAPbCl_3)$ perovskites show the characteristic band-edge absorption of the 3D $MAPbCl_3$ perovskite around 420 nm, and additionally the feature exciton absorption peak (around 329 nm) associated with the 2D mono-layered perovskite appears in the spectra of both $AVA(MAPbCl_3)$ and $AVA_2(MAPbCl_3)$. Again, these behaviors differ essentially from the previous report of 2D/3D $AVA(MAPbBr_3)_n$ perovskites, in which quasi-2D phases containing different numbers of Pb–Br octahedral layers and thus having different band gaps exhibited exciton absorption peaks at varying wavelengths.[24] The PL features of the $MAPbCl_3$ and $AVA_x(MAPbCl_3)$ perovskites are illustrated in Fig. 3b. Typically, the 3D $MAPbCl_3$ perovskite displays a band-edge emission peak at ∼403.77 nm. Interestingly, $AVA_{0.125}(MAPbCl_3)$ and $AVA_{0.25}(MAPbCl_3)$ perovskites show similar band-edge emissions overlapped with a red-shifted band at 412 and 418 nm, respectively. Additionally, two emission peaks in the visible region are observed at 549 and 701 nm in $AVA_{0.125}(MAPbCl_3)$ and $AVA_{0.25}(MAPbCl_3)$ perovskites, which are attributable to defect states in the 2D perovskite phase.[13] Moreover, the $AVA(MAPbCl_3)$ perovskite displays a band-edge emission

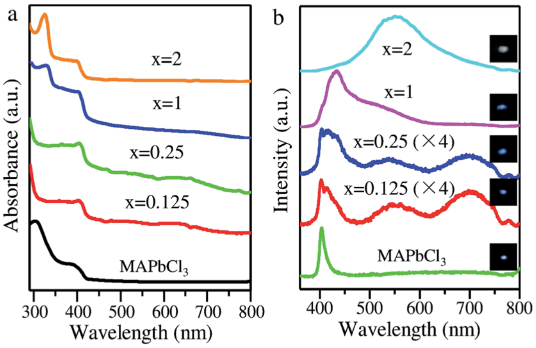

Fig. 3 Absorption (a) and steady-state (b) photoluminescence spectra of $MAPbCl_3$ and $AVA_x(MAPbCl_3)$ perovskites. The luminous photographs of $AVA_x(MAPbCl_3)$ under 325 nm xenon lamp irradiation are inset on each photoluminescence spectrum.

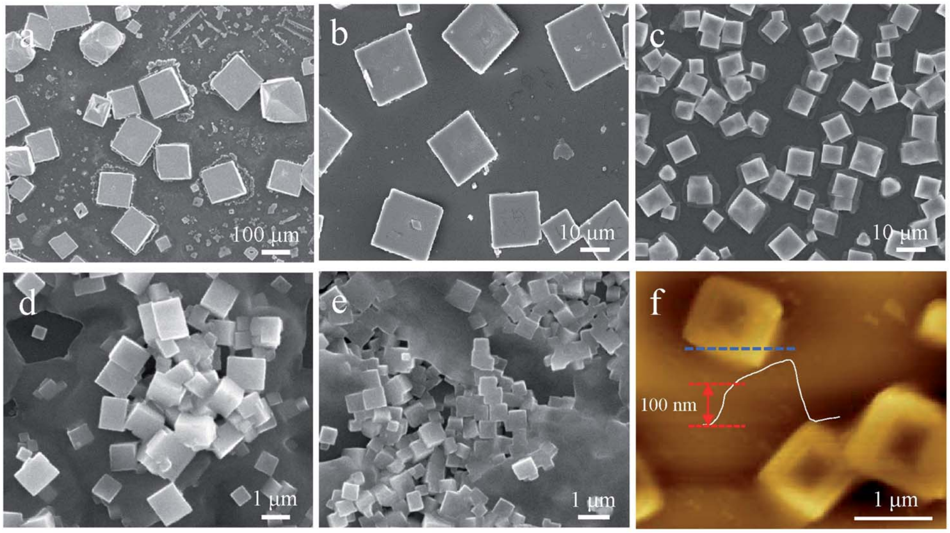

Fig. 2 Morphology of $MAPbCl_3$ and $AVA_x(MAPbCl_3)$ perovskites. SEM images of $MAPbCl_3$ (a) and $AVA_x(MAPbCl_3)$ perovskites with $x = 0.125$ (b), $x = 0.25$ (c), $x = 1$ (d) and $x = 2$ (e). (f) AFM topography of the $AVA_2(MAPbCl_3)$ perovskite.

peaking at 434 nm, which is overlapped with broad emission at long wavelengths. The broad emission is attributed to the transient self-trapped exciton (STE) states that are generated in the distorted lattice of the formed 2D mono-layered perovskites.[27] The band-edge emission and STE emission jointly enable the broadband emission of the AVA($MAPbCl_3$) perovskite. Particularly, the AVA_2($MAPbCl_3$) perovskite exhibits ultrabroad emission spanning the entire visible spectrum with a maximum at ∼550 nm and a full width at half-maximum (FWHM) of 127 nm (0.95 eV). The broadband white emission with a large Stokes shift is similar to the white emission reported previously in 2D perovskites, which originated from the growing STEs in a highly distorted crystal lattice.[27] Obviously, the PL of the AVA_x($MAPbCl_3$) perovskite evolves from narrow band-edge emission over additional discrete defect-state emission to broadband white emission as the structural dimensionality decreases from 3D to mixed-dimensional. Herein, we ascribe the structure dimensionality dependent broadband emission in AVA_x($MAPbCl_3$) perovskites to the STEs generated in distorted Pb–Cl octahedra, which are caused by the insertion of bilayers of the 5-AVA molecule and Pb–COO^- coordination.[28] Impressively, AVA_x($MAPbCl_3$) perovskites have much higher PL intensity than the 3D $MAPbCl_3$ perovskites, indicating strong exciton emission from the natural quantum well structure. Notably, the AVA_2($MAPbCl_3$) perovskite achieves the maximum PL intensity, resulting from the strongest quantum confinement effect in the 2D mono-layered perovskite.

Actually, the AVA_2($MAPbCl_3$) perovskite has intense emission in the blue visible region, resulting in a "cold" white-light emission with a correlated color temperature (CCT) of 8624 K (Fig. 4a). Also, the emission has chromaticity coordinates (CIE) of (0.28, 0.33), which deviate from the white-light point (0.33, 0.33) due to the additional contribution of the blue emission. However, the deviation from the white-light point of the AVA_2($MAPbCl_3$) perovskite emission is much smaller than that of (*N*-MEDA)$PbBr_{3.5}Cl_{0.5}$ (ref. 10) and (EDBE)$PbCl_4$ (ref. 29) perovskites, indicating a superior white-light emission of AVA_2($MAPbCl_3$). Moreover, the AVA_2($MAPbCl_3$) perovskite emitted light has a color rendering index (CRI) of 85, comparable to that of many commercially available LEDs. The inset photograph in Fig. 4a shows the white emission from the AVA_2($MAPbCl_3$) perovskite under the excitation of a 325 nm laser. The PL lifetime of an individual AVA_2($MAPbCl_3$) submicron platelet was measured by time-resolved PL spectroscopy. As shown in Fig. 4b, the decay curve shows a bi-exponential feature with lifetimes of 2.87 ns (54%) and 0.43 ns (46%), which are comparable to those of other 2D perovskites.[30]

Based on the above observations, we conclude that 5-AVA has a critical effect on the formation of AVA_x($MAPbCl_3$) submicron platelets. To reveal the underlying growth and dimensionality transformation mechanism, we further employed several bi-functional organic molecules to manipulate the dimensionality transformation and growth of perovskites. Fig. 5a–c show the SEM images of the bi-functional organic molecule modulated perovskites. Apparently, both the pentanedioic acid ($COOH(CH_2)_3COOH$) and citric acid ($(COOHCH_2)_2COHCOOH$) modulated perovskites display lateral dimensions of ∼20 μm, much smaller than those of $MAPbCl_3$ perovskites (Fig. 5a, b, and 2a). However, the 4-amino-1-butanol ($OH(CH_2)_4NH_2$) modulated perovskites display a cuboid shape with lateral dimensions of ∼20 μm (Fig. 5c). Based on the above observations, we conclude that functional cations with –COOH/–OH groups that facilitate Pb–O coordination are critical in inhibiting the growth of perovskites. Nevertheless, the zwitterionic 5-AVA molecule is found to be the most efficient surfactant in inhibiting the growth of 3D $MAPbCl_3$ perovskites. Herein, we deduce that the 5-AVA molecules preferably bond to Pb atoms rather than Cl atoms *via* Pb–COO^- coordination, slowing down the vertical growth rate and yielding perovskite submicron platelets.[31] Then, XRD measurements were performed for further structure confirmation (Fig. 5d–f). Obviously, pentanedioic acid and citric acid modulated perovskites show typical (001) and (002) diffraction peaks that can be assigned to 3D $MAPbCl_3$ perovskites, indicating no structure transformation (Fig. 5d and e). In contrast, the zwitterionic 4-amino-1-butanol modulated perovskite displays a series of (00*l*) diffraction

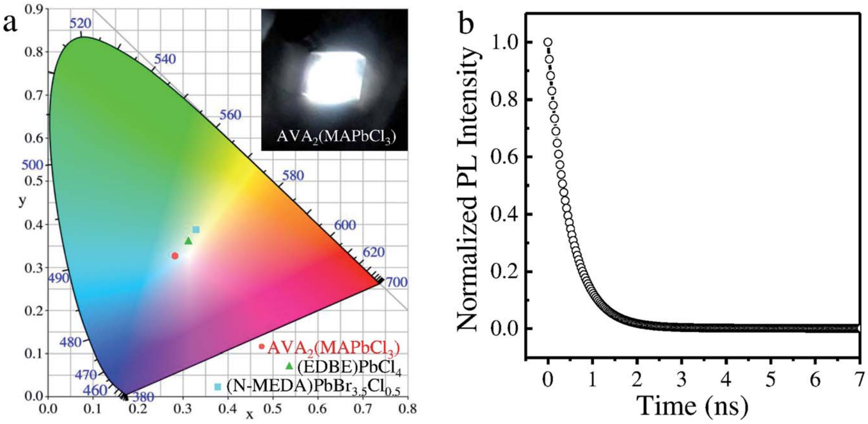

Fig. 4 (a) Chromaticity coordinates of the emissions in a 1931 color space chromaticity diagram. The inset is a white light emission picture of the AVA_2($MAPbCl_3$) perovskite irradiated under a 325 nm laser. (b) Time-resolved PL decay of the AVA_2($MAPbCl_3$) perovskite recorded at an emission wavelength of 355 nm.

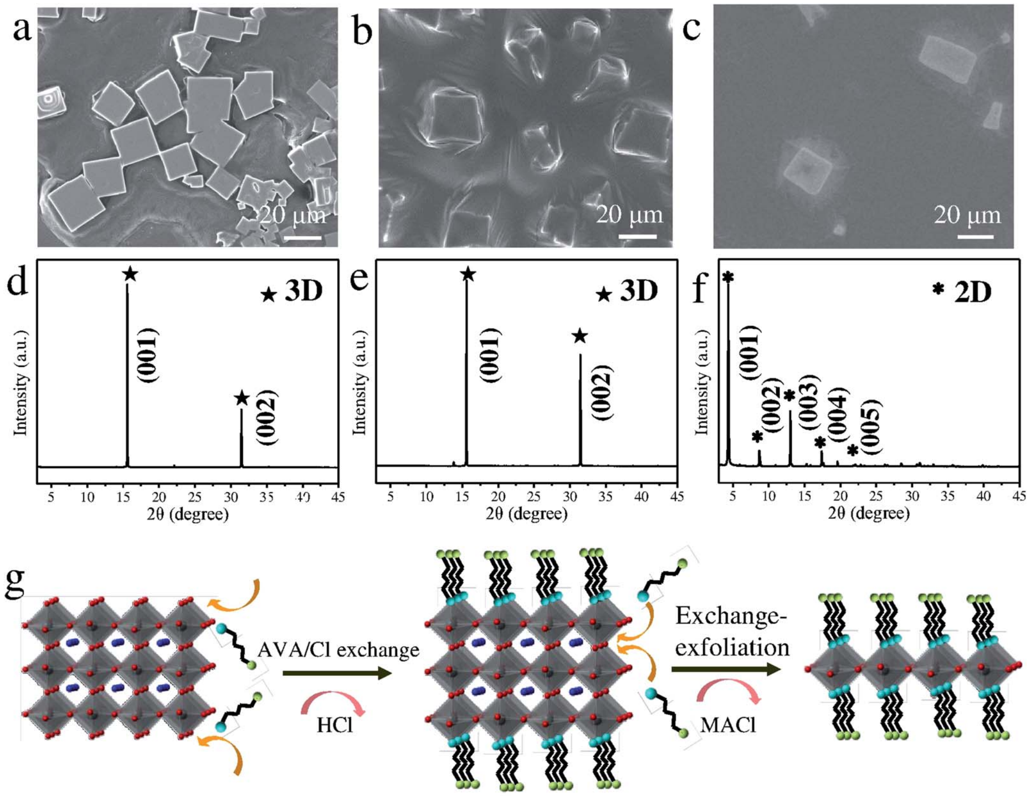

Fig. 5 SEM images of pentanedioic acid (a), citric acid (b) and 4-amino-1-butanol (c) stabilized perovskites. XRD patterns of pentanedioic acid (d), citric acid (e) and 4-amino-1-butanol (f) stabilized perovskites. (g) Schematic illustration of the 5-AVA induced structural dimensionality transformation mechanism.

peaks attributable to the 2D mono-layered phase and weak (001) and (002) diffraction peaks from the 3D phase, confirming the formation of mixed-dimensional perovskites (Fig. 5f). Thus, it is concluded that organic molecules with zwitterionic groups are crucial for facilitating the transformation of 3D perovskites into mixed-dimensional perovskites. The proposed mechanism illustrating the dimensionality transformation is depicted in Fig. 5g. Typically, the formation mechanism involves a Pb–COO^- coordination directed exchange reaction and a subsequent exfoliation process. Upon 5AVA/Cl exchange reactions occurring at the two ends of the Cl sites of Pb–Cl octahedra, 3D perovskites are exfoliated into 2D multilayered perovskites, with volatile HCl released into air. Further exchange reactions occur at the vertex-shared Cl sites of Pb–Cl octahedra, accompanied by the release of MACl. Once the exchange reaction between the bilayers of the 5AVA molecule and the two ends of Cl sites in a single Pb–Cl octahedral layer occurs, 2D multilayered perovskites would be further exfoliated into 2D mono-layered perovskites. Notably, the number of quantum well layers (*i.e.*, Pb–Cl octahedral layers) for $AVA_x(MAPbCl_3)$ perovskites is highly dependent on the intercalation of 5-AVA.

To identify whether the $AVA_2(MAPbCl_3)$ perovskite differs from the 2D mono-layered AVA_2PbCl_4 perovskite, we then fabricated a 2D AVA_2PbCl_4 perovskite *via* a conventional method for comparison. The crystal structure of the 2D AVA_2PbCl_4 perovskite is displayed in Fig. S2a,† where inorganic layers of corner-sharing $[PbCl_6]^{4-}$ octahedra are confined between interdigitating bilayers of intercalated $AVAH^+$. Here, the $AVAH^+$ cations are attached to the Pb–Cl network *via* hydrogen bonds. A series of (00*l*) diffraction peaks appeared in the XRD pattern (Fig. S2b†) confirming the 2D RP phase of the AVA_2PbCl_4 perovskite, which differs from the mixed-dimensional $AVA_2(MAPbCl_3)$ perovskite. Besides, the 2D AVA_2PbCl_4 perovskite exhibits a typical lamellar morphology (Fig. S2c†) with a thickness of ~190 nm (Fig. S2d†), much thicker than the $AVA_2(MAPbCl_3)$ submicron platelets. The disparities in the morphology and structure indicate that the Pb–COO^- coordination greatly affects the growth of the $AVA_2(MAPbCl_3)$ perovskite. Despite the structure and morphology disparities, the 2D AVA_2PbCl_4 perovskite shows similar exciton absorption (318 nm) (Fig. S3a†) and broadband emission (Fig. S3b†) to the $AVA_2(MAPbCl_3)$ perovskite. The observed similar properties suggest that the surface Pb–COO^- bonding has little effect on the electronic structure of the $AVA_2(MAPbCl_3)$ perovskite.

Another appealing characteristic of the mixed-dimensional $AVA_x(MAPbCl_3)$ perovskite submicron platelets is their superior stability. Time-dependent XRD characterization suggests that the structure of the $AVA_2(MAPbCl_3)$ perovskite undergoes no obvious degradation after storage for 30 days under ambient conditions (Fig. S4a†). Moreover, time-dependent PL measurement reveals that the PL intensity decreased to 75% of the initial value after storage for 30 days under ambient conditions, indicating a fairly good stability of optical properties.

4. Conclusions

In summary, we have developed a facile approach for fabricating mixed-dimensional perovskite submicron platelets. The introduction of 5-AVA into the $MAPbCl_3$ perovskite precursor simplified the synthesis and enabled the structural dimensionality and morphology transformation. Notably, a structural dimensionality dependent broadband emission is observed, suggesting that the emission originates from self-trapped excitons (STEs). The $AVA_2(MAPbCl_3)$ perovskite exhibits white-light emission with a color rendering index (CRI) of 85 and a correlated color temperature (CCT) of 8624 K, yielding “cold” white light. It is proposed that 5-AVA molecules bonded to Pb^{2+} ions suppress the vertical growth and lead to the lateral growth of submicron platelets. And an exchange and exfoliation mechanism for understanding the 5-AVA directed dimensionality transformation is elaborated. Furthermore, the $AVA_x(MAPbCl_3)$ perovskite exhibits good structure and light-emission stability after storage for 30 days under ambient conditions. Overall, the facile synthesis strategy will offer exciting opportunities for the development of low-dimensional perovskite nanostructures for the creation of a wide range of optoelectronic devices.

Conflicts of interest

There are no conflicts to declare.

Acknowledgements

This work was supported by the National Key R&D Program of China (Grant No. 2019YFB1503500), the National Natural Science Foundation of China (21805075, 51572073, 11774082), the Natural Science Foundation of Hubei Province, China (2018CFB176, 2019CFA006), the Program for Science and Technology Innovation Team in Colleges of Hubei Province (T201901), and Wuhan Application Foundation Frontier Project (No. 2018010401011287).

References

1 A. Kojima, K. Teshima, Y. Shirai and T. Miyasaka, *J. Am. Chem. Soc.*, 2009, **131**, 6050–6051.

2 G. E. Eperon, T. Leijtens, K. A. Bush, R. Prasanna, T. Green, J. T. Wang, D. P. McMeekin, G. Volonakis, R. L. Milot, R. May, A. Palmstrom, D. J. Slotcavage, R. A. Belisle, J. B. Patel, E. S. Parrott, R. J. Sutton, W. Ma, F. Moghadam, B. Conings, A. Babayigit, H. G. Boyen, S. Bent, F. Giustino, L. M. Herz, M. B. Johnston, M. D. McGehee and H. J. Snaith, *Science*, 2016, **354**, 861–865.

3 J. H. Tong, Z. N. Song, D. H. Kim, X. H. Chen, C. Chen, A. F. Palmstrom, P. F. Ndione, M. O. Reese, S. P. Dunfield, O. G. Reid, J. Liu, F. Zhang, S. P. Harvey, Z. Li, S. T. Christensen, G. Teeter, D. W. Zhao, M. M. Al-Jassim, M. F. A. M. V. Hest, M. C. Beard, S. E. Shaheen, J. J. Berry, Y. F. Yan and K. Zhu, *Science*, 2019, **364**, 475–479.

4 S. Bai, P. M. Da, C. Li, Z. P. Wang, Z. C. Yuan, F. Fu, M. Kawecki, X. J. Liu, N. Sakai, J. T.-W. Wang, S. Huettner, S. Buecheler, M. Fahlman, F. Gao and H. J. Snaith, *Nature*, 2019, **571**, 245–250.

5 Y. Cao, N. N. Wang, H. Tian, J. S. Guo, Y. Q. Wei, H. Chen, Y. F. Miao, W. Zou, K. Pan, Y. R. He, H. Cao, Y. Ke, M. M. Xu, Y. Wang, M. Yang, K. Du, Z. W. Fu, D. C. Kong, D. X. Dai, Y. Z. Jin, G. Q. Li, H. Li, Q. M. Peng, J. P. Wang and W. Huang, *Nature*, 2018, **562**, 249–253.

6 N. N. Wang, L. Cheng, R. Ge, S. T. Zhang, Y. F. Miao, W. Zou, C. Yi, Y. Sun, Y. Cao, R. Yang, Y. Q. Wei, Q. Guo, Y. Ke, M. T. Yu, Y. Z. Jin, Y. Liu, Q. Q. Ding, D. W. Di, L. Yang, G. C. Xing, H. Tian, C. H. Jin, F. Gao, R. H. Friend, J. P. Wang and W. Huang, *Nat. Photonics*, 2016, **10**, 699–704.

7 H. H. Tsai, W. Y. Nie, J. C. Blancon, C. C. Stoumpos, R. Asadpour, B. Harutyunyan, A. J. Neukirch, R. Verduzco, J. J. Crochet, S. Tretiak, L. Pedesseau, J. Even, M. A. Alam, G. Gupta, J. Lou, P. M. Ajayan, M. J. Bedzyk, M. G. Kanatzidis and A. D. Mohite, *Nature*, 2016, **536**, 312–316.

8 M. J. Yuan, L. N. Quan, R. Comin, G. Walters, R. Sabatini, O. Voznyy, S. Hoogland, Y. B. Zhao, E. M. Beauregard, P. Kanjanaboos, Z. H. Lu, D. H. Kim and E. H. Sargent, *Nat. Nanotechnol.*, 2016, **11**, 872–877.

9 L. Pedesseau, D. Sapori, B. Traore, R. Robles, H. H. Fang, M. A. Loi, H. Tsai, W. Y. Nie, J. C. Blancon, A. Neukirch, S. Tretiak, A. D. Mohite, C. Katan, J. Even and M. Kepenekian, *ACS Nano*, 2016, **10**, 9776–9786.

10 E. R. Dohner, E. T. Hoke and H. I. Karunadasa, *J. Am. Chem. Soc.*, 2014, **136**, 1718–1721.

11 L. L. Mao, Y. L. Wu, C. C. Stoumpos, M. R. Wasielewski and M. G. Kanatzidis, *J. Am. Chem. Soc.*, 2017, **139**, 5210–5215.

12 L. L. Mao, P. J. Guo, M. Kepenekian, I. Hadar, C. Katan, J. Even, R. D. Schaller, C. C. Stoumpos and M. G. Kanatzidis, *J. Am. Chem. Soc.*, 2018, **140**, 13078–13088.

13 L. T. Dou, A. B. Wong, Y. Yu, M. L. Lai, N. Kornienko, S. W. Eaton, A. Fu, C. G. Bischak, J. Ma, T. Ding, N. S. Ginsberg, L.-W. Wang, A. P. Alivisatos and P. D. Yang, *Science*, 2015, **349**, 1518–1521.

14 A. Yangui, D. Garrot, J. S. Lauret, A. Lusson, G. Bouchez, E. Deleporte, S. Pillet, E. E. Bendeif, M. Castro, S. Triki, Y. Abid and K. Boukheddaden, *J. Phys. Chem. C*, 2015, **119**, 23638–23647.

15 K. Thirumal, W. K. Chong, W. Xie, R. Ganguly, S. K. Muduli, M. Sherburne, M. Asta, S. Mhaisalkar, T. C. Sum, H. S. Soo and N. Mathews, *Chem. Mater.*, 2017, **29**, 3947–3953.

16 L. L. Mao, Y. L. Wu, C. C. Stoumpos, B. Traore, C. Katan, J. Even, M. R. Wasielewski and M. G. Kanatzidis, *J. Am. Chem. Soc.*, 2017, **139**, 11956–11963.

17 C. M. Ji, S. S. Wang, L. N. Li, Z. H. Sun, M. C. Hong and J. H. Luo, *Adv. Funct. Mater.*, 2019, **29**, 1805038.

18 A. Y. Mei, X. Li, L. F. Liu, Z. L. Ku, T. F. Liu, Y. G. Rong, M. Xu, M. Hu, J. Z. Chen, Y. Yang, M. Grätzel and H. W. Han, *Science*, 2014, **345**, 295–298.

19 W. Y. Nie, H. Tsai, R. Asadpour, J.-C. Blancon, A. J. Neukirch, G. Gupta, J. J. Crochet, M. Chhowalla, S. Tretiak, M. A. Alam, H. L. Wang and A. D. Mohite, *Science*, 2015, **347**, 522–525.

20 S. T. Williams, F. Zuo, C.-C. Chueh, C.-Y. Liao, P.-W. Liang and A. K.-Y. Jen, *ACS Nano*, 2014, **136**, 13249–13256.

21 W. J. Ke, G. J. Fang, J. W. Wan, H. Tao, Q. Liu, L. B. Xiong, P. L. Qin, J. Wang, H. W. Lei, G. Yang, M. C. Qin, X. Z. Zhao and Y. F. Yan, *Nat. Commun.*, 2015, **6**, 6700.

22 L. L. Mao, Y. L. Wu, C. C. Stoumpos, B. Traore, C. Katan, J. Even, M. R. Wasielewski and M. G. Kanatzidis, *J. Am. Chem. Soc.*, 2017, **139**, 11956–11963.

23 Z. W. Zhuang, C. D. Peng, G. Y. Zhang, H. M. Yang, J. L. Yin and H. H. Fei, *Angew. Chem., Int. Ed.*, 2017, **56**, 14411–14416.

24 T. Y. Zhang, L. Q. Xie, L. Chen, N. J. Guo, G. Li, Z. Q. Tian, B. W. Mao and Y. X. Zhao, *Adv. Funct. Mater.*, 2017, **27**, 1603568.

25 Y. C. Liu, Z. Yang, D. Cui, X. D. Ren, J. K. Sun, X. J. Liu, J. R. Zhang, Q. B. Wei, H. B. Fan, F. Y. Yu, X. Zhang, C. M. Zhao and S. Z. F. Liu, *Adv. Mater.*, 2015, **27**, 5176–5183.

26 D. H. Cao, C. C. Stoumpos, O. K. Farha, J. T. Hupp and M. G. Kanatzidis, *J. Am. Chem. Soc.*, 2015, **137**, 7843–7850.

27 M. D. Smith and H. I. Karunadasa, *Acc. Chem. Res.*, 2018, **51**, 619–627.

28 G. Grancini and M. K. Nazeeruddin, *Nature*, 2019, **4**, 4–20.

29 E. R. Dohner, A. Jaffe, L. R. Bradshaw and H. I. Karunadasa, *J. Am. Chem. Soc.*, 2014, **136**, 13154–13157.

30 J. N. Chen, Y. G. Wang, L. Gan, Y. B. He, H. Q. Li and T. Y. Zhai, *Angew. Chem.*, 2017, **129**, 15089–15093.

31 G. H. Ahmed, J. Yin, R. Bose, L. Sinatra, E. Alarousu, E. Yengel, N. M. Alyami, M. I. Saidaminov, Y. H. Zhang, M. N. Hedhili, O. M. Bakr, J.-L. Bredas and O. F. Mohammed, *Chem. Mater.*, 2017, **29**, 4393–4400.